Sea ice emissivity modelling at L-band and application to Pol-Ice 2007 campaign field data

Peter Mills, Georg Heygster, *Fellow, IEEE,*

***Abstract*—Sea ice emissivity models for the L-band frequency range are described, then tested on Pol-Ice campaign field measurements. Pol-Ice was conducted in March 2007 in the N. Baltic in preparation for the launch of the Soil Moisture and Ocean Salinity (SMOS) instrument, a satellite microwave radiometer operating at 1.4 GHz. The campaign comprised airborne measurements from the EMIRAD L-band radiometer and the E-M Bird ice thickness meter. Because of the translucency of sea ice at L-band, it is hoped that SMOS will render information on ice thickness. Three variations on radiative transfer are used to model EMIRAD brightness temperatures from collocated E-M Bird measurements: a single, plane-parallel model, an ensemble of such models, and a ridged, Monte Carlo model based on geometric optics that includes both the top and bottom surface topography. All three models accurately account for the instrument antenna pattern, relevant to satellite-mounted radiometers which sample a large and heterogeneous area. Because of ice growth processes, salinity, and by extension, permittivy, is a partial function of ice thickness; thus the models are further refined so that permittivity varies with ice thickness, which was necessary to correctly model the polarization difference. Other issues related to effective permittivities, an intermediate quantity in the models, are discussed. Analysis of partial correlations show that ice ridging makes a significant contribution to the measured signal, commending further study using scattering models more appropriate to the scale of the ridging relative to wavelength.**

***Index Terms*—**

I. INTRODUCTION

It is now widely recognized that sea ice plays a significant role in the global climate. Monitoring both its extent and exchange processes is the challenge facing us in an uncertain twenty-first century. Passive microwave sensors are an excellent tool for the task. Amongst their advantages are frequent, global coverage in most or all weather conditions, and a lengthy record. The main disadvantage is a relatively poor horizontal resolution.

Recently, a new microwave radiometer called Soil Moisture and Ocean Salinity (SMOS) was launched. As its name implies, the chief focus of this instrument will be the pedosphere and the ocean surface. Information will be rendered nonetheless when it is pointing at the cryosphere instead. SMOS is unique in measuring in the L-band range at 1.4 GHz, the first continuously operating passive instrument to do so. It will also be capable of detecting all four Stokes components. The angular field of view (FOV) of an antenna is directly proportional to the wavelength and inversely proportional to the effective aperture area. By using a broad array of antennas that fold out upon deployment, SMOS will have a horizontal resolution comparable to other microwave radiometers despite operating at a lower frequency [1]. Synthetic apertures will be generated by correlating the signals from each detector.

P. Mills and G. Heygster are both with the Institute of Environmental Physics, University of Bremen, Otto-Hahn-Allee 1, 28359 Bremen, Germany, e-mail: pmills@iup.physik.uni-bremen.de.

Manuscript received July 21, 2010

Because sea ice is quite translucent (penetration depths can be 2 m or more [2]) at L-band, at least some knowledge of the internal structure of the sea ice, thickness and salinity in particular, will be rendered. Monitoring these quantities is important to climate scientists since both are important determinants of surface heat-flux and salt- and freshwater-fluxes.

To facilitate the design of retrieval algorithms, forward emissivity models that generate correct predictions will be invaluable. Here we test several such models against field data from the Pol-Ice campaign conducted in March of 2007 in the Northern Baltic. The Pol-Ice campaign included measurements from a fully polarimetric, L-band radiometer as well as measurements of both the ice surface and ice-water interface. Menashi et al. [3] were able to relate brightness temperature to ice thickness for a UHF radiometer operating at 611 MHz using a simple, three-layer dielectric slab emissivity model. We use a similar model to demonstrate such a relationship at L-band but with two important refinements: accounting for ice ridging and for the dependence of permittivity on ice thickness.

II. THEORY

A. Plane-parallel radiative transfer model

Sea ice is a complex composite comprised primarily of ice crystals, included pockets of brine and air bubbles [4]. These granular structures will act to scatter radiation and produce a substance with quite different electro-magnetic properties than those of its constituent components. Because the size of the scatterers (on the order of 1 mm) relative to the wavelength (about 20 cm) is quite small, volume scattering in L-band is weak [5]. Vant, Ramseier and Makios [6] estimate that volume scattering will only be significant above 1.5 GHz for multi-year ice and 24 GHz for first-year ice, based on Rayleigh theory calculations. A similar result can also be generated more rigorously from simulations based on strong fluctuation theory (SFT) [7], [8].

Therefore, to simulate sea ice emissivities, we confine ourselves to radiative transfer simulations with specular reflection at the interfaces and bulk electromagnetic properties calculated in the low-frequency limit. At its simplest, such a model would comprise the Fresnel equations, which return reflection coefficients for a discontinuous interface between

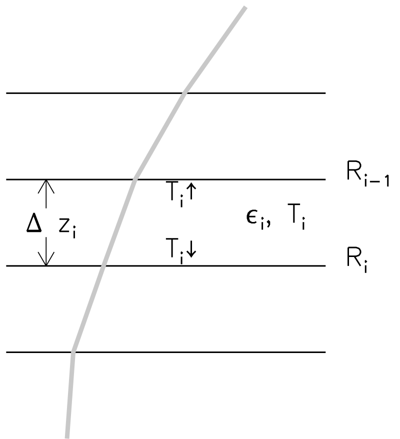

Fig. 1. Geometry of a radiative transfer model for layered, discontinuous, plane-parallel media.

two dielectrics and are derived by imposing continuity of the electric and magnetic fields:

$$R_{vi} = \left[\frac{n_{i+1}\cos\theta_i - n_i\cos\theta_{i+1}}{n_{i+1}\cos\theta_i + n_i\cos\theta_{i+1}}\right]^2 \quad (1)$$

$$R_{hi} = \left[\frac{n_i\cos\theta_i - n_{i+1}\cos\theta_{i+1}}{n_i\cos\theta_i + n_{i+1}\cos\theta_{i+1}}\right]^2, \quad (2)$$

where R_{pi} is the complex reflection coefficient for polarisation p (*h*orizontal or *v*ertical), n_i and n_{i+1} are the complex refractive indices of the top (incoming wave) and bottom (transmitted wave) substance respectively. θ_i is the angle of incidence and θ_{i+1} is the transmission angle, calculated via Snell's law:

$$n_i \sin\theta_i = n_{i+1}\sin\theta_{i+1}. \quad (3)$$

Since sea ice is non-magnetic, the refractive index can be calculated from relative permittivity only:

$$n_i = \sqrt{\epsilon_i}. \quad (4)$$

While such a model can be useful at higher frequencies where the penetration depth is small (the ice is optically thick) [9], [10], sea ice is quite translucent at L-band, thus we need to take into account its internal structure, the ice-water interface for thin ice in particular. A schematic diagram of a multi-layer, plane-parallel radiative transfer model with discontinuous interfaces is shown in Figure 1. Because of the plane-parallel geometry, the angle of all reflected rays in a given layer will be the same. Upwelling and down-welling components of the brightness temperature ($T_i \uparrow$ and $T_i \downarrow$, respectively) are defined for each layer and we can relate them to the layer properties by summing each of the contributions. This produces the following sparse, linear system:

$$T_i\uparrow - \tau_i(1-R_i)T_{i+1}\uparrow - \tau_i R_i T_i\downarrow = (1-\tau_i)T_i \quad (5)$$

$$T_i\downarrow - \tau_i(1-R_{i-1})T_{i-1}\downarrow - \tau_i R_{i-1} T_i\uparrow = (1-\tau_i)T_i, \quad (6)$$

where T_i is the physical temperature of the ith layer and τ_i is its transmission coefficient, which can be derived using Beer's law:

$$\tau_i = \exp\left(-\frac{\alpha_i \Delta z_i}{\cos\theta_i}\right), \quad (7)$$

where Δz_i is the layer thickness and α_i is the attenuation coefficient:

$$\alpha_i = \frac{4\pi\nu}{c}\mathrm{imag} n_i, \quad (8)$$

where ν is the frequency and c is the speed of light.

For the boundary conditions, we set $\epsilon_1 = 1$, $T_1\downarrow = T_{sky}$ and $T_m\uparrow = T_w$ where T_{sky} is the sky brightness temperature and T_w is the physical temperature of the lowermost layer, normally water. In other words, the topmost layer is the open air and the bottom layer is assumed to be infinitely optically thick.

While coherency effects have been observed in thin ice of fairly uniform thickness [11], by throwing out the phase components of both the transmission and the reflection coefficients, we have produced here what is known as an *incoherent solution*. This is more appropriate in the real world of ice remote sensing in which ice thickness is highly variable over the instrument footprint.

As is the case for measurements from the Pol-Ice campaign, we may have no knowledge of the internal structure of the ice sheet. By assuming uniform properties within, we arrive at the following, closed-form solution to the system of equations in (5) and (6):

$$T_b = \frac{(R_{ia}-1)\left\{\begin{array}{c}\left[R_{wi}\tau^2 + (1-R_{wi})\tau - 1\right]T_{ice} + \\ (R_{wi}-1)\tau T_w + (R_{ia}-1)R_{wi}\tau^2 T_{sky}\end{array}\right\}}{(R_{ia}R_{wi}\tau^2 - 1)}, \quad (9)$$

where T_b is the measured brightness temperature, R_{ia} is the reflection coefficient at the ice-air interface, R_{wi} is the reflection coefficient at the water-ice interface, T_{ice} is the ice temperature and T_w is the water temperature.

B. Monte Carlo ridged ice model

Most ice emissivity models assume plane-parallel geometry, with permittivity varying solely across depth. Yet in ocean emissivity modelling, it is well understood how both small- and large- scale roughness affect the emitted radiation [12], [13]. Like the ocean, sea ice will also have rough interfaces, not only with the air, but also with the water. In particular, ridging will affect the signal by changing the effective viewing angle.

To account for this effect, a simple, two-dimensional, ray-tracing, Monte Carlo model was designed based on geometric optics. The functional relation with depth for both the ice-air and water-ice interfaces is assumed to be known, as is the case for the Pol-Ice measurements. The ray is traced backwards, from the instrument head to the ice sheet. When it encounters an interface (either ice-air or water-ice) it is either reflected back or refracted into the new material with the probability equal to the reflection coefficient as determined by the Fresnel equations. Once the ray encounters no further interfaces it is initialized with the temperature of its current material—either ice, air or water—and a radiative transfer calculation

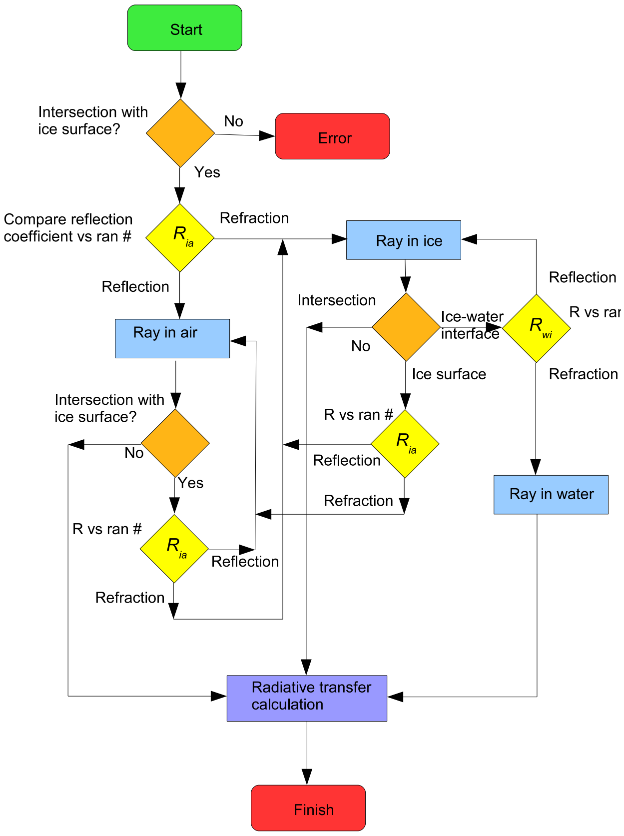

Fig. 2. Flow diagram describing Monte Carlo ray-tracing algorithm.

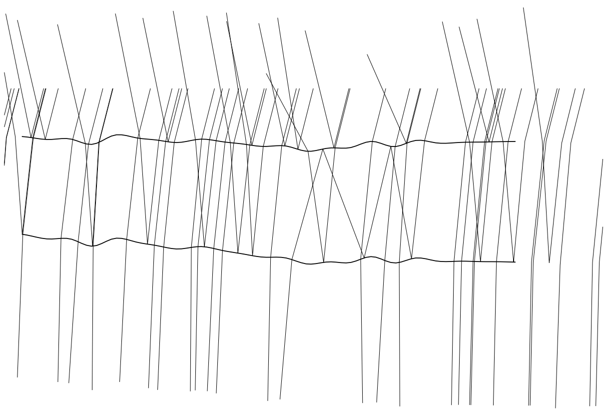

Fig. 3. An example of a single ray-tracing simulation. Incoming rays have been truncated at a constant depth.

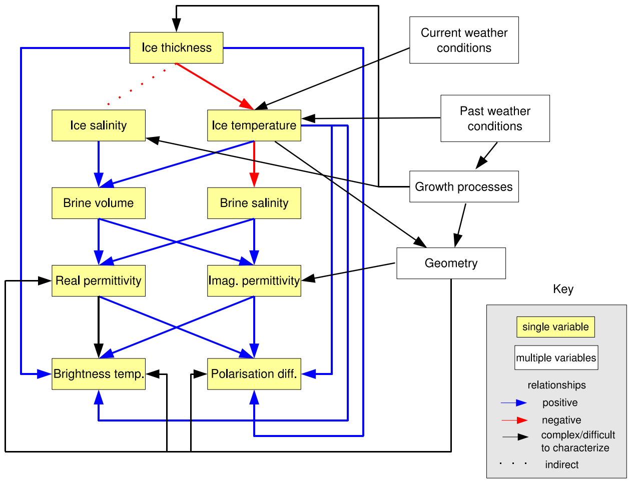

Fig. 4. Diagram showing the inter-dependencies of the different quantities determining the final, measured brightness temperature of sea ice. Blue arrows indicate direct, positive, monotonic relationships. Red arrows are direct, inverse, monotonic relationships. Black arrows are more complex relationships. Dotted lines are indirect relationships.

performed in the opposite direction:

$$\frac{dI(s)}{ds} = \alpha(s)\left[T(s) - I(s)\right], \tag{10}$$

where I is the brightness temperature of the radiation along the path, s, α is the attenuation coefficient and T is the physical temperature. Note that the reflection terms are not included in this integration; they are implicitly accounted for through the random direction on encountering an interface. The final brightness temperature at the instrument head is estimated by tracing many rays and averaging the results.

To better understand the procedure, a flow-diagram describing the algorithm for tracing a single ray is shown in Figure 2, while a plot of an actual simulation is shown in Figure 3.

C. *Mixture models of effective permittivity*

The most important step in emissivity models of this type is the calculation of effective permittivity. Because volume scattering is weak at L-band due to the small size of the scatterers, mixture models based on the low-frequency limit would appear to be more appropriate than more involved models such as SFT. Two types of mixture models may be distinguished: those that take as input only the brine volume, and those that require calculation of brine permittivity. In the former case, we have the empirical formulas of Vant et al. [6] in which the effective permittivity is linearly related to brine volume:

$$\epsilon^* = mV_b + k, \tag{11}$$

where ϵ^* is real or imaginary permittivity, V_b is brine volume and m and k are constants. Another example is the following formula for real permittivity:

$$\epsilon' = \frac{\epsilon_{pi}}{1 - 3V_b}, \tag{12}$$

found in Hoekstra and Capillino [14]. Here, ϵ_{pi} is the permittivity of pure ice.

More involved formulas require knowledge of the permittivity of the inclusion material (in this case brine). Representative formulas can be found in Sihvola and Kong [15] and Shokr [16]. Once we admit brine permittivity, the functional dependencies become quite complex, as illustrated in Figure 4. Because the brine is always at or near its freezing point, brine salinity is a function of temperature only: the more saline the brine, the lower its freezing point. We use the empirical, piecewise-continuous polynomial relationship given in Ulaby et al. [17], Appendix E-5.1, to calculate brine salinity. So long as the ice is not too porous, brine volume can be approximated from brine salinity:

$$V_b \approx \frac{S_b(T)}{S}, \tag{13}$$

where S is ice salinity and S_b is the brine salinity.

That leaves the dielectric constant of the brine. This is a complex function of frequency, temperature and salinity, a formula for which can be found in Ulaby et al. [17] based on Debye relaxation curves but will not be repeated here. The same formula, or a similar one, will also be needed to calculate the permittivity of sea water for the lowest layer of the emissivity model.

The difficulty with mixture formulas is that there are many different ones producing widely divergent results as will be treated in more depth in Section V-B. They also require at least some knowledge of inclusion geometry which is generally lacking. Golden [18] shows a method of generating rigorous bounds on the effective permittivity for a two-component dielectric medium through analytic continuation [19]. These bounds delineate the range of reasonable effective permittivity values for a given brine volume mixed in pure ice and for any possible micro-structural arrangement of brine inclusions.

By the analytic continuation method, the bounds on effective permittivity, ϵ^*, are represented by two arcs. The first is given by:

$$\epsilon_2(1 - V_b) - (\epsilon_2 - \epsilon^*)z = (\epsilon_2 - \epsilon^*)s, \tag{14}$$

where z is a parameter between 1 and $1 - V_b$. The second is given by:

$$\frac{\epsilon_1}{\epsilon^*} = 1 - \frac{V_b}{s - z} \tag{15}$$

Here, z is a parameter between 1 and V_b. V_b is the volume of inclusion material (brine), ϵ_1 is the permittivity of the host material (ice), ϵ_2 is the permittivity of the inclusion material (brine), and $s = 1/(1 - \epsilon_1/\epsilon_2)$.

III. Data

A. Pol-Ice campaign

The Pol-Ice campaign was conducted in March 2007 over the Bay of Bothnia in the Northern Baltic. It comprised two components: point-to-point and circular flyovers by an airplane carrying the fully polarimetric EMIRAD radiometer [20] operating at L-band, and point-to-point flyovers by a helicopter towing an ice thickness detector called the E-M Bird. The E-M Bird instrument detects the ice-water transition using inductance variations in a pair of electromagnetic coils (similar to a metal-detector) while the ice surface height is measured with a laser altimeter [21].

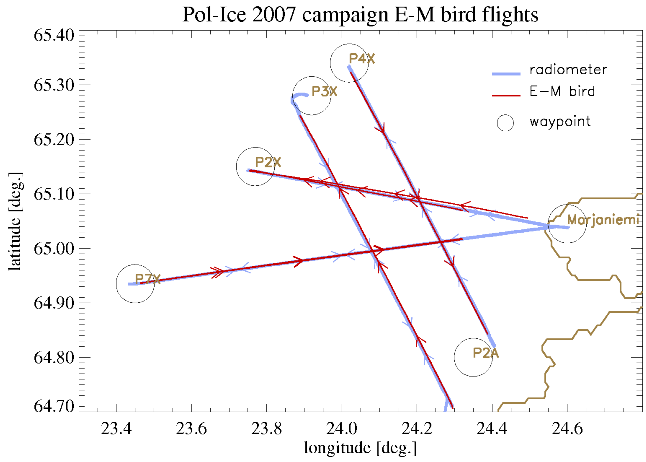

Fig. 5. Summary of Pol-Ice 2007 E-M Bird overflights with coincident EMIRAD overfights.

The inductance meter of the E-M Bird instrument samples at a rate of 10 Hz, which translates to a data-point spacing of between 2 and 4 m, while the laser altimeter, at 100 Hz, samples at ten times the rate. The footprint size of the inductance meter is estimated at around 40 m [21], while the LIDAR footprint is estimated at between 10 and 20 cm. Because of attenuation of the radiation as it travels through the ice, the more highly-resolved top surface should be most important in determining the emitted radiance.

The coincident measurements from EMIRAD and E-M Bird are summarized in Figure 5. Flights are labelled based on the way-points. EMIRAD flights were also designated by a number: all radiometer flights are summarized in Figure 9. Weather conditions during the campaign found temperatures at or above freezing with overcast skies and patches of fog. Only data from the first two Stokes components (horizontally polarised brightness temperature, T_{bh}, and vertically polarised brightness temperature, T_{bv}) from the aft-looking (mounted 40 degrees with respect to the aircraft vertical axis) antenna will be used in this study.

B. Processing and collocation procedures

Because the radiometer was fixed on the aircraft, its pointing direction will be affected by changes in aircraft attitude, which must be corrected for for accurate collocations. The following equations give the measurement coordinate as a function of the aircraft coordinates and attitude—pitch, roll and yaw:

$$\begin{aligned}
\zeta' &= P + \zeta && (16)\\
dx &= z \tan \zeta' && (17)\\
dy &= z \sin R && (18)\\
\psi &= \psi_a + \frac{1}{r_E \sin \psi_a}(dx \cos H + dy \cos H) && (19)\\
\phi &= \phi_a + \frac{1}{r_E}(dx \cos H - dy \sin H), && (20)
\end{aligned}$$

where P is the aircraft pitch, $\zeta = 40°$ is the instrument looking angle relative to the aircraft longitudinal axis, R is the aircraft roll, $(\psi_a,\ \phi_a)$ are the longitude, latitude coordinates of the aircraft, z is altitude, H is the heading r_E is the radius of the Earth and $(\psi,\ \phi)$ are the ground coordinates of the measurement center.

The same geometrical approach can be used to figure out the effective viewing angle. Many formulations are possible. Here is one of them:

$$\theta_1 = \sin^{-1}\sqrt{\tan^2\zeta' + \sin^2 R}. \tag{21}$$

To simplify the analysis, an approximate conversion to Cartesian coordinates was applied, with the X coordinate denoting distance along the flight path while the Y is distance across it:

$$\begin{aligned} X_0 &= r_E(\theta-\theta_0)\cos\phi & (22)\\ Y_0 &= r_E(\phi-\phi_0) & (23)\\ \gamma &= \tan^{-1}(\Delta\psi, \Delta\theta\cos\bar{\phi}) & (24)\\ X &= X_0\cos\gamma + Y_0\sin\gamma & (25)\\ Y &= -X_0\sin\gamma + Y_0\cos\gamma, & (26)\end{aligned}$$

where $\Delta\theta = \theta_f - \theta_0$ is the total longitudinal travel of the reference flight track, $\Delta\phi = \phi_f - \phi_0$ is the total latitudinal travel and $\phi = (\phi_0 + \phi_f)/2$ is the average latitude of the reference flight track. To collocate two or more approximately overlapping flight tracks, the transformation is applied first to a reference flight, the coefficients saved and the same transformation applied to all others. Distances can easily be calculated in two ways: since the X coordinate will vary much faster than the Y, for fast, crude collocations, a one-dimensional distance can be calculated based only on difference in the X dimension, while for more accurate collocations, we use the standard Cartesian metric.

C. EMIRAD instrument characteristics

Brightness temperature measurements will be affected not only by what is there, but also by the instrument characteristics. The half-power FOV of the EMIRAD instrument for the aft-looking geometry is 31 degrees, translating to a footprint size of over 250 m for a 500 m cruising altitude. This is much broader than the E-M Bird footprint, therefore we account for the smearing produced by the EMIRAD instrument by weighting each of the thickness measurements based on its power-response function.

The angle from the instrument boresight direction, δ, of a given ice thickness measurement can be calculated:

$$\delta = \cos^{-1}\left[\frac{(\mathbf{r_a}-\mathbf{r})\cdot(\mathbf{r_a}-\mathbf{r_t})}{|\mathbf{r_a}-\mathbf{r}||\mathbf{r_a}-\mathbf{r_t}|}\right], \tag{27}$$

where $\mathbf{r} = (X, Y, 0)$ is the radiometer measurement location, $\mathbf{r_a} = (X_a,\ Y_a,\ z)$ is the aircraft position and $\mathbf{r_t} = (X_t,\ Y_t,\ 0)$ is the ice thickness measurement location. The power-response function of the instrument is a Gaussian with respect to the angle from the instrument boresight direction [20]:

$$w = \exp\left(\frac{\delta}{2\sigma_{FOV}}\right), \tag{28}$$

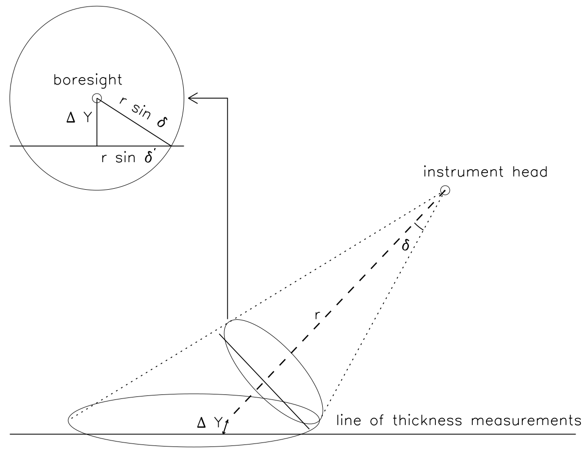

Fig. 6. Diagram showing how to convert angle from instrument boresight to an equivalent angle along a line of measurements offset from the footprint center.

where σ_{FOV} is the angular FOV of the instrument and w is used to weight the thickness measurements for collocation with a given radiometer measurement:

$$\begin{aligned} W &= \sum_i w_i & (29)\\ \bar{d} &= \frac{1}{W}\sum_i d_i w_i, & (30)\end{aligned}$$

where $\{d_i\}$ are the set of ice thickness measurements, $\bar{d}$ is the average over the instrument footprint while the radiometer measurement location is held constant. The sum of the weights, W, gives the equivalent number of thickness samples within the radiometer footprint and can be used to screen the quality of the collocation by admitting only those values larger than a certain threshold.

Since the algorithm to calculate thickness from E-M Bird measurements assumes infinite water depth [21], some of the thickness measurements were flagged because of shallow water. These were similarly averaged to form a "shallow water fraction."

The instrument power-response function will also need to be simulated in the Monte Carlo model by generating random deviates for the angle at the instrument head. It would seem a straightforward matter to simply generate Gaussian deviates, however EMIRAD and E-M Bird measurements are not always perfectly coincident. Consider the measurement geometry shown in Figure 6 in which we need deviates along a line offset from the instrument boresight. We can transform normal deviates for the overall offset angle, δ to a corrected offset angle, δ' as follows:

$$\delta' = \mathrm{sgn}\delta\sin^{-1}\sqrt{\sin^2\delta - (\Delta Y/r)^2}, \tag{31}$$

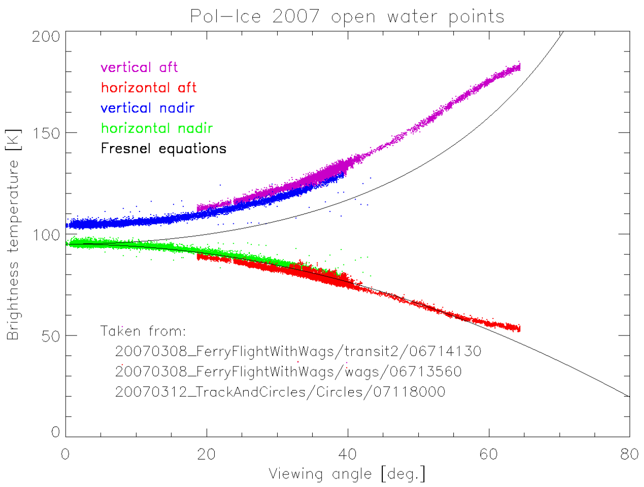

Fig. 7. Measured (points) versus model (lines) brightness temperatures over open water as a function of viewing angle. Points with excessive polarization mixing, caused by large aircraft roll angles (one of the open water flights has a zig-zag pattern) have been filtered out.

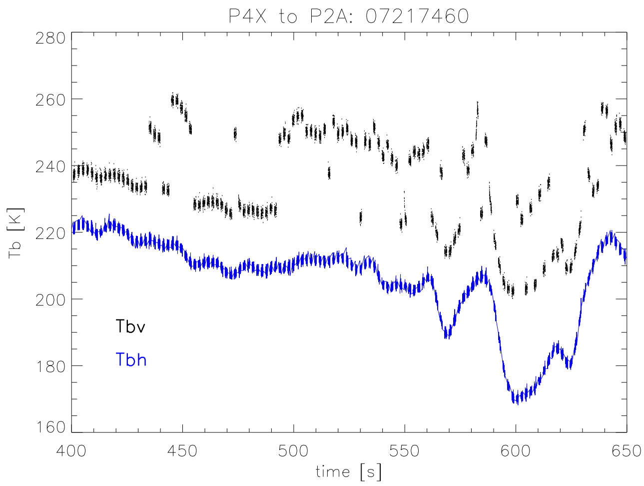

Fig. 8. Detail of P4X to P2A flight showing shifting of calibration offset in the vertical polarisation.

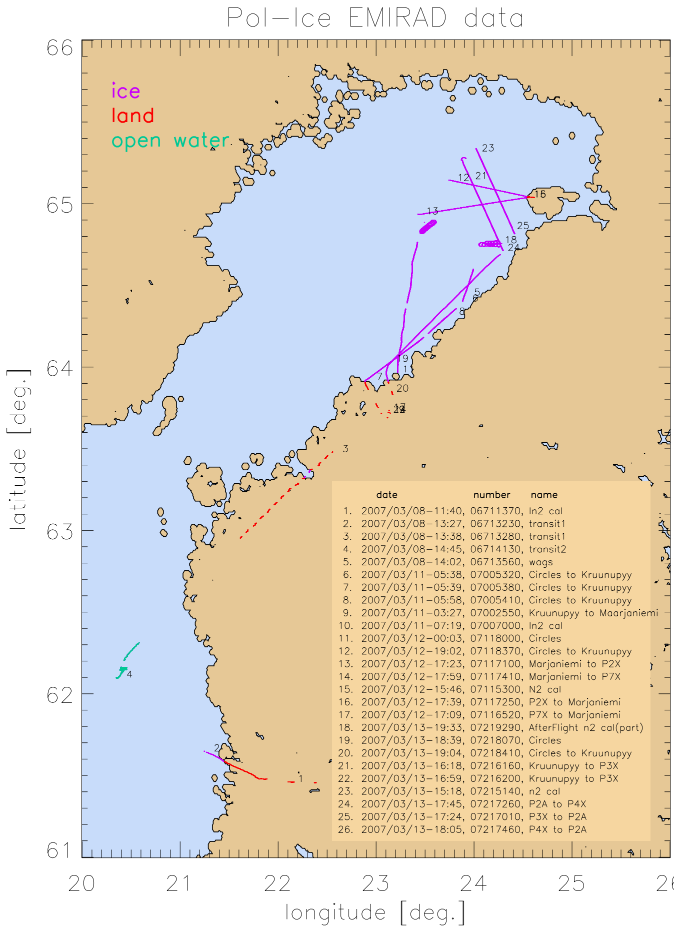

Fig. 9. Map of all Pol-Ice EMIRAD measurements showing surface-type. Open water points were derived from ASI high-resolution sea ice concentrations. Land points were filtered using a land-mask, which is also drawn as coastline. Flights are labelled by date, name and number. Study area can be seen in the upper right corner.

where $\Delta Y/r$ is the offset distance of the line of measurements from the footprint center normalized by the distance from the instrument head. All deviates for which $\sin|\delta| < \Delta Y/r$ or $|\delta| < \sin^{-1}(\Delta Y/r)$ will need to be discarded. This can be done by generating uniform deviates within a certain range and then transforming them to normal deviates by inverting the error function. The out-of-plane contribution to the incidence angle is ignored.

D. Calibration errors

As Figure 7 shows, there was a considerable discrepancy between the measured and modelled radiance values over open water, especially in the vertical polarisation. Open water points were derived from the ARTIST Sea Ice algorithm (ASI) [22] by taking ice concentrations of less than 1 %. Since the horizontal and vertical polarisations do not agree at the 0 degree viewing angle, it was assumed that this was due to an offset calibration error in the radiometer. In addition, it is apparent from Figure 8, which shows a detail of one of the Pol-Ice EMIRAD flights, that this calibration offset was not always constant. The trace shows large discontinuities that are not likely due to changes in surface type. These shifts occur only in the vertical polarisation and produce both a large polarisation difference and high radiance that do not appear even physically possible.

Since the open water points were so far distant—over 300 km—from the collocated thickness measurements and were performed four and five days prior (8th versus the 12th and 13th), it is unlikely that calibration offsets derived from the open water points will be applicable. Anomalous spiking was also observed, primarily within the vertical channel [23].

Because of these calibration errors, measurements and results derived from them must be treated with some caution. While it might appear from Figure 8 that the bad data can be removed, further examination of the data shows that the radiometer was not just jumping, but actually wandering. Little can be done about this—the data was presented “as is.” If statistical relationships can be demonstrated, however, they

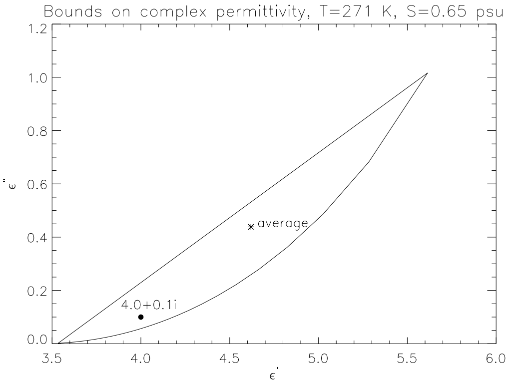

Fig. 10. Bounds on effective permittivity for approximate campaign conditions: freezing conditions (T_{ice}=272 K, S=0.65), low ice salinity.

will occur despite errors in the data, with the calibration problems providing an extra source of random variation or a further unknown variable. In the particular case of modelling the polarisation difference, correlations must occur *in spite of* rather than because of the calibration problems—this will be treated in more detail in Section IV-C. Therefore we feel that the concepts treated within are valid and that emissivitiy calculations show meaningful statistical relationships with measured values.

IV. RESULTS

A. Constant permittivity

Weather conditions during the campaign found temperatures at or above freezing with overcast skies and patches of fog. While the salinity of the Baltic, particularly the Northern Baltic, is much lower than that of the oceans, so long as the salinity of the parent water is greater than 0.6 psu, ice formed from it structurally resembles that of more saline bodies, with preferred crystal orientations and brine inclusions [24].

The brine in first-year sea ice at melting conditions will have a highly irregular geometry. Brine inclusions will form drainage channels [4], the geometry of which will be difficult to predict. There may also be melt-puddles on the top surface in addition to a layer of "skim," composed of snow saturated with highly saline brine. Since the measurements were taken during melting conditions and since the emissivity models being used represent the sea ice in a very crude manner (with no knowledge of the internal structure of the ice, which is, after all, lacking), we cannot make any assumptions as to the geometry of the brine inclusions, and take brine volume as our only constraint.

Figure 10 shows the bounds calculated from analytic continuation for the approximate conditions encountered during the campaign: freezing conditions and low ice salinity. The average is shown by the star while the value used to run the model, $\epsilon = 4.0 + 0.1i$, is shown by the black circle. This value was chosen because it produced a good correlation with measured values.

The ice emissivity models were tested against measured radiances for a pair of selected, coincident EMIRAD and E-M bird meter overflights —flight number 07216200: Krunuupyy to P3X and flight P2A to P3X, respectively—see Figures 5 and 9. The time series are shown in Figure 11 while scatter diagrams are plotted in Figure 12 for 5000 randomly chosen EMIRAD measurement points against three different models. In the scatter diagrams, points flagged for shallow water (shallow water fraction ¿ 0.1) as well as those with too few thickness measurements ($W < 50$) in the center of the footprint are removed—see Section III-C.

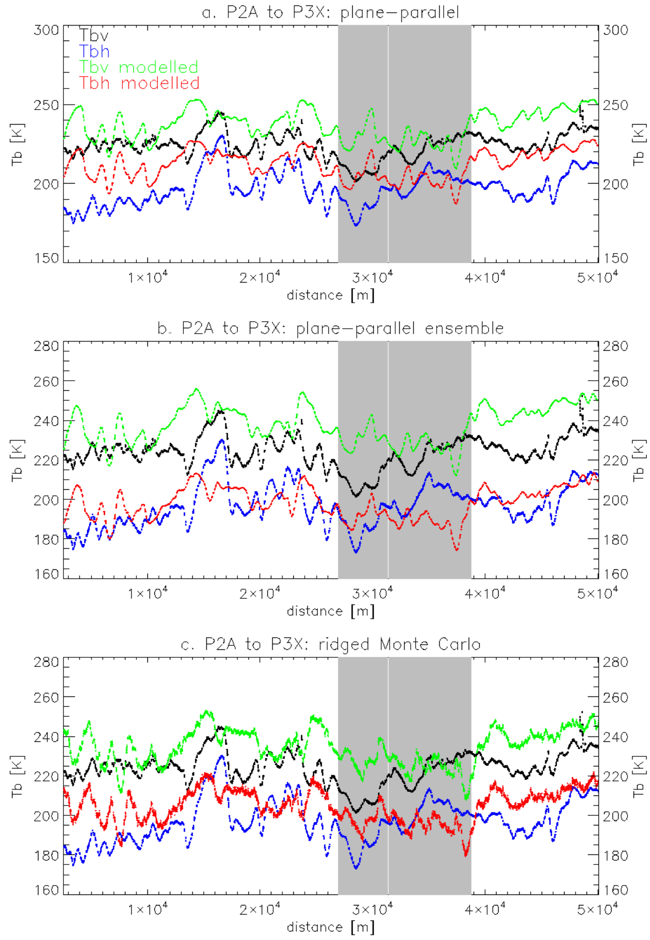

Fig. 11. Time series showing model results versus measurements for a pair of EMIRAD and E-M bird overflights (number 07216200 and P2A to P3X). Three different models were used: a three-layer, plane-parallel model, an ensemble of plane-parallel models averaged over the instrument footprint and a ridged Monte Carlo, ray-tracing algorithm. Shading shows E-M bird points flagged for shallow water. A constant permittivity of $\epsilon = 4.0 + 0.1i$ was assumed.

The first model is the three-layer, plane-parallel model given by Equation (9). Input to the model is ice thickness averaged over the instrument footprint as described in Section III-C, an ice temperature of 272 K, a water temperature of 273 K and a water salinity of 5 psu. The last two correspond to a water permittivity of 83.0+18.3i. The second model is also a plane-parallel model, except instead of first averaging the ice thickness and angle of incidence over the footprint, the model is run for each measurement point in the footprint and the results averaged in the same manner. The final model is the ridged Monte Carlo model described in Section II-B. To generate each estimate, 20000 rays were traced between the

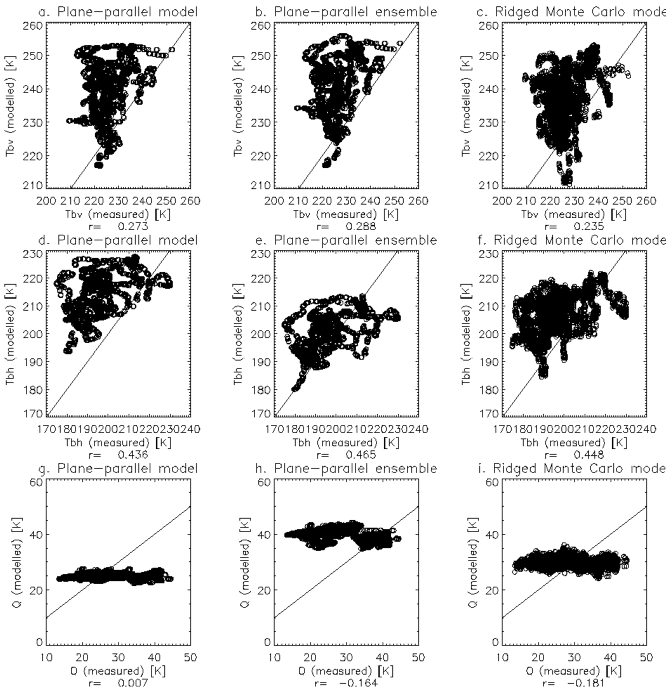

Fig. 12. Scatter plots showing model results versus measurements for a pair of EMIRAD and E-M bird overflights (number 07216200 and P2A to P3X). Three different models were used: a three-layer plane-parallel model, an ensemble of plane-parallel models averaged over the instrument footprint and a ridged Monte Carlo ray-tracing algorithm. A constant permittivity of $\epsilon = 4.0 + 0.1i$ was assumed.

water-ice and ice-air interfaces interpolated from the E-M bird measurements using a cubic spline [25].

Correlations are slightly improved in the horizontal for both ridged models versus the single plane-parallel model and slightly in the vertical for the ensemble of models. For the single model, correlation of the polarisation difference (or second Stokes component, $Q = T_{bv} - T_{bh}$) is negligible, while for the ridged models it is actually negative. In order to improve predictions in the second Stokes component, permittivity needs to vary with ice thickness which will be addressed in the next two sections.

These results also show a considerable improvement over older results (not shown here) in which the antenna pattern was modelled as a simple, box-car average over the line of measurements (or uniform deviates for the Monte Carlo model). Thus it is important to properly characterise the instrument response when performing forward model calculations, especially in the case of satellite-mounted radiometers which sample over a very broad and typically heterogeneous area.

The polarisation signal for both ridged ice models is higher, on average, than that for the single model. This can be understood by inspection of Figure 7: the rate of change of polarisation difference with respect to incidence angle increases with increasing angle—the same is true for emissivities over ice. Higher and lower angles are equally weighted in the ensemble as implied in Equations (28) and (30) or for a more visual demonstration, in Figure 6, thus the final moment is biased towards higher values of polarisation difference.

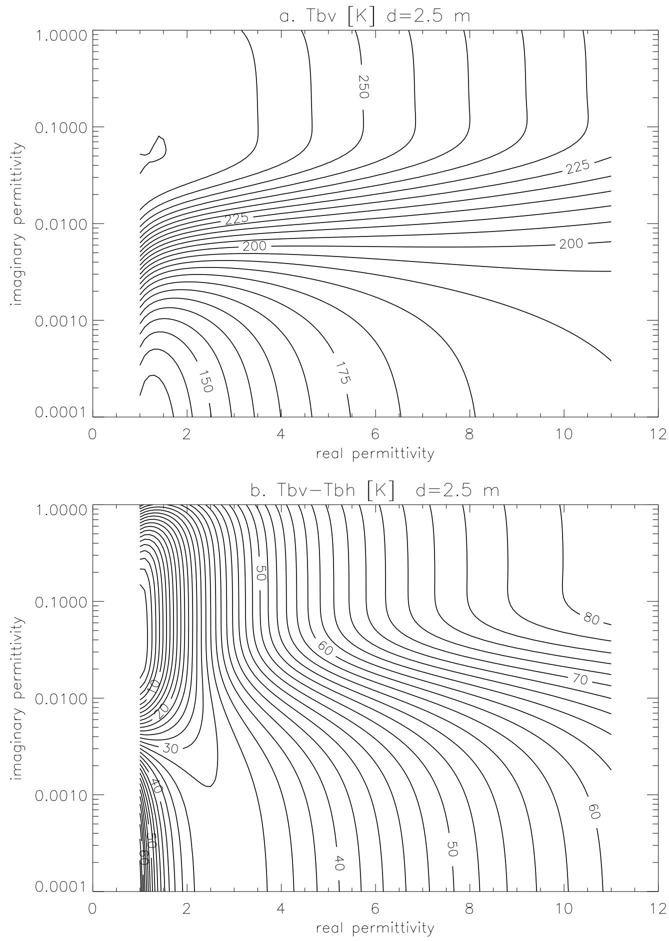

Fig. 13. Emitted brightness temperature as a function of complex permittivity according to the emissivity model (9) for an ice temperature of 265K. The incidence angle is 45 degrees.

B. Retrieval of effective permittivities

It is now well understood how ice salinity, particularly surface salinity, is related to ice thickness through of growth processes [4], [26], [27]. First, because thin ice conducts heat more quickly, it freezes faster, meaning that less brine is expelled and, second, brine drainage and expulsion processes reduce the salt content of old ice [28]–[30]. Since the higher permittivities of more saline ice produce both a lower emissivity and a higher polarisation difference, Martin et al. [31] as well as Naoki et al. [10] use this property to estimate ice thickness from passive microwave measurements. We hypothesize that the same feature is also present in the less saline ice of the Baltic and demonstrate such a relationship using permittivity estimates derived from the Pol-Ice campaign data. Because of changing weather conditions, ice growth is highly variable regardless of thickness, thus there is much uncertainty in the thickness-salinity relationship. Since thinner ice conducts heat more quickly, it will tend to be warmer, i.e. closer to the water temperature, which will also act to increase permittivities. Because of the freezing conditions during the campaign, this is not an issue here.

Figure 13 shows a plot of the brightness temperature and polarisation difference as a function of the complex permit-

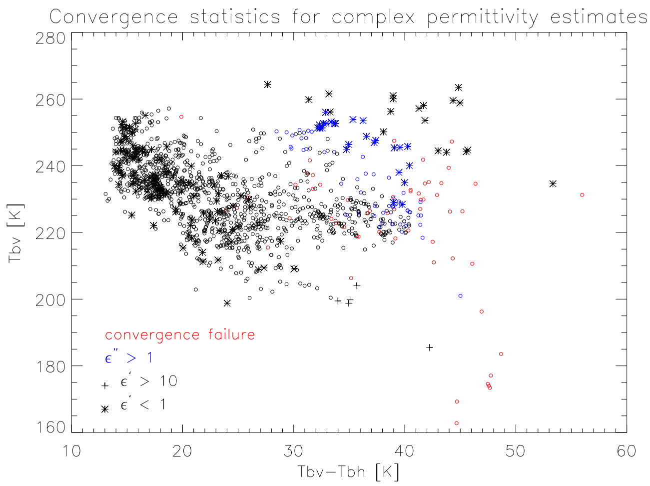

Fig. 14. Convergence of complex permittivity estimates in measurement space. Red points have failed to converge. Blue points have converged but have an imaginary permittivity greater than one. Crosses have a real permittivity greater than ten, while asterisks have a real permittivity of less than one. Convergence, in this case, is defined as a summed square error of less than 1 K.

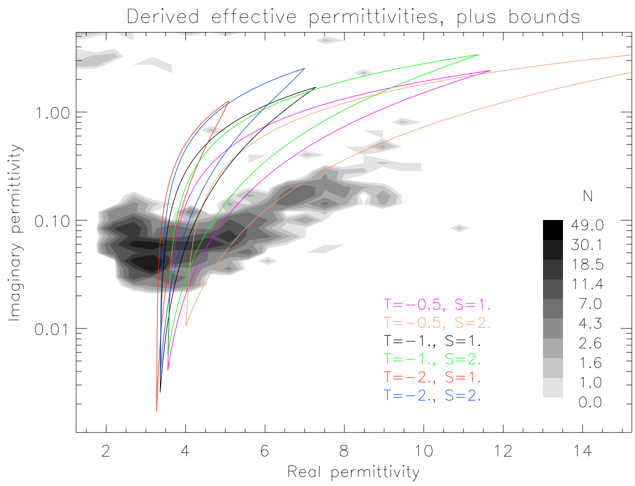

Fig. 15. Derived effective permittivities from Pol-Ice campaign plus bounds calculated from analytic continuation. Temperatures in the figure are given in degrees Celsius while salinities are in psu.

tivity for a 2.5 m thick ice sheet at 265 K. Especially within the central region of the plots, it is apparent that if all other parameters in the equation are known, inverting (9) to determine the complex permittivity from the measured brightness temperature is quite a well-posed problem. Consider: pick a given isoline in one plot, another one in the other and they will likely have a unique intersection. The central region determines the transition zone between ice that is transparent and ice that is opaque, hence it is exactly the region of interest because of the translucency of sea ice at L-band. It can be understood from Figure 13a as follows: in transparent ice (bottom of plot), a higher real permittivity will increase the brightness temperature because there are more reflections within the ice layer. Conversely, as the ice becomes optically thick (top of plot), a higher real permittivity will decrease the brightness temperature because the ice now reflects more down-welling radiation from the sky.

The operation of the radiometer was cyclic, taking a cluster of measurements every 2 seconds as seen in Figure 8. Averaging each cluster has several advantages: first, by removing points with a standard deviation greater than a certain threshold (10 K), many anomalous spikes, caused by a malfunction in the radiometer, may be discarded. Second, instrument noise is reduced thus the measurement becomes more stable. Finally, the smaller data set is far easier to work with and process. Further quality checks were applied: the equivalent number of thickness measurements, W, had to be greater than 1000, while the shallow water fraction had to be less than 0.01 (less than 1 % of thickness measurements in the footprint were affected by shallow water)—see Section III-C. The modelled overflight, P2A to P3X, was also excluded. As described in the next section, a thickness-permittivity relation will be derived from the results and cross-validated by using it in the radiative transfer models in the chosen overflight.

Equation (9) was inverted using an iterated, stochastic algorithm: several points are randomly chosen from a bounded region, the forward model is applied and the point with the smallest error chosen. The bounded region is reduced in size and the process repeated until the error is smaller than a predefined tolerance. In addition to being faster, this algorithm converged more reliably than a downhill simplex [25]. Ice and water temperatures were the same as used in Section IV-A in the forward model, 272 and 273 K, respectively. Since bad values will be thrown away, we need to carefully examine the convergence statistics to avoid introducing a selection bias. Figure 14 shows that all but a few points have converged and generated sensible estimates. While the instrument calibration errors mean they are likely not reliable in and of themselves, these estimates should nonetheless be useful for generating statistics. Figure 15 compares the effective permittivity estimates with bounds calculated by analytic continuation for representative ice conditions.

C. *Varying permittivity with ice thickness*

Figure 16 shows the dependence of permittivity on ice thickness with the lines illustrating fits of the form:

$$\epsilon^* = \exp(ad + b) + c, \tag{32}$$

where d is ice thickness and a, b and c are constants.

When these fits are applied to the models, the correlation of modelled versus measured polarisation difference improves notably—the scatter plots in Figure 18 now display an upward slope. The time series is shown in Figure 17. The ridged models show a slight improvement over the single, plane-parallel model only in the horizontal channel. Polarisation difference is also negatively correlated with brightness temperature as shown in Figures 14 and 19a. (In the latter figure, this negative correlation is somewhat obscured by the calibration errors.) This can occur only if the ice is, in general, optically thick and with a variable real permittivity (see discussion in section in Section IV-B and Figure 13), conditions that are now met: Figure 19 shows that varying permittivity with ice

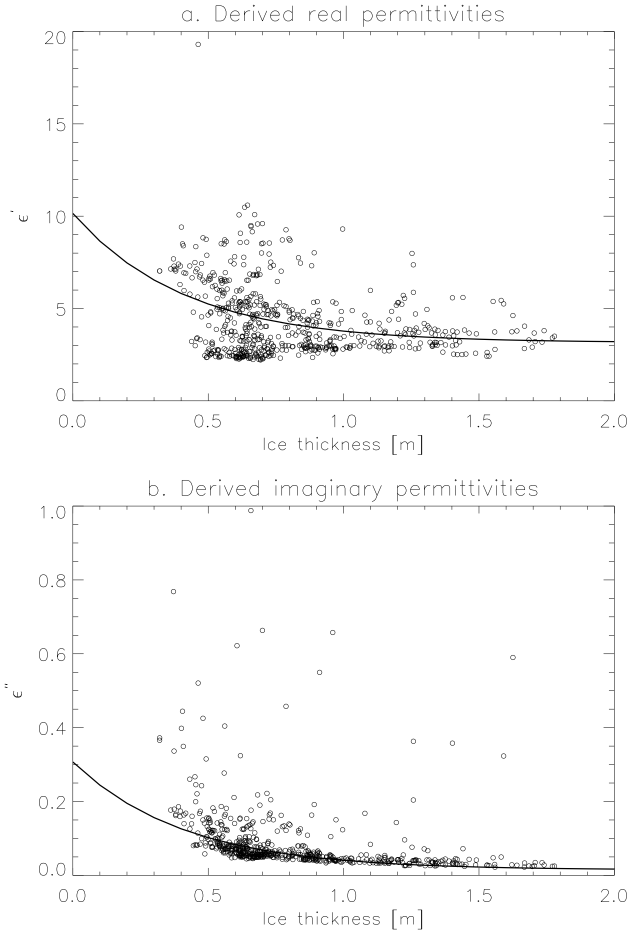

Fig. 16. Derived permittivity versus ice thickness with fitted exponentials.

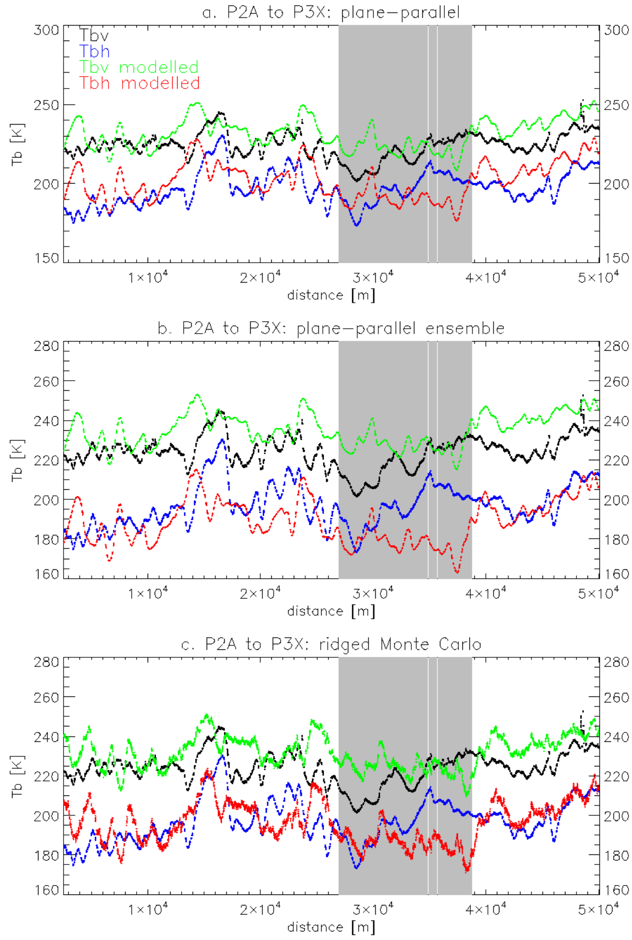

Fig. 17. Same as Figure 11 except varying permittivity with ice thickness.

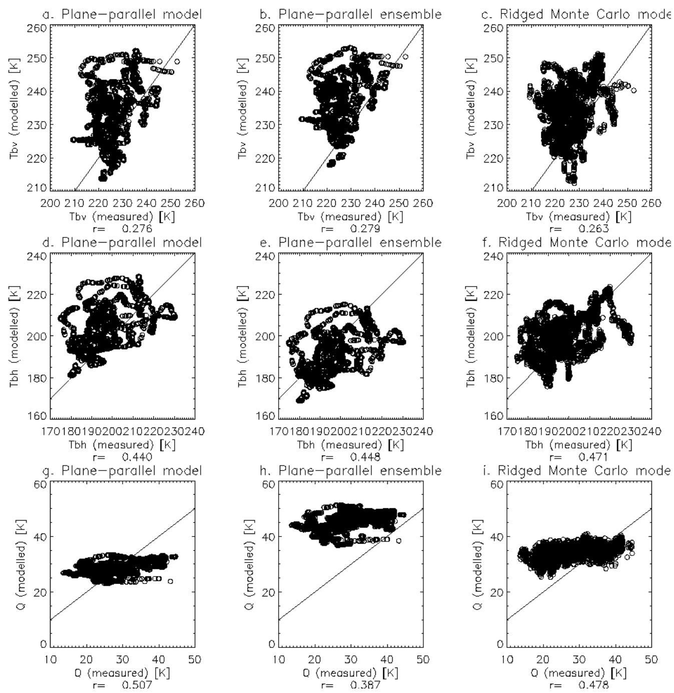

Fig. 18. Same as Figure 12 except varying permittivity with ice thickness.

thickness correctly predicts the negative correlation between brightness temperature and polarisation difference. With a constant permittivity, the models predict a positive correlation between brightness temperature and polarisation difference. Thus the polarisation signal explains some of the variance in brightness temperature and vice versa. Note that because the calibration problems affected only the vertical channel, they will tend to obscure these relationships rather than accidentally producing them.

V. Discussion

Figures 19 through 21 are scatter plots illustrating the functional dependencies—brightness temperature versus polarization difference, brightness temperature versus thickness and polarization difference versus thickness, respectively—for the measured radiances and for the three different models all using the exponential permittivity-thickness relation. Very little scatter is seen in the single, plane-parallel model, while the two ridged models, especially the Monte Carlo model, have much larger scatter that is more in line with the measurements. A small part of the scatter—less than 1. K—seen in the Monte Carlo model will be the result of using a stochastic algorithm: While the ridged ice models may not predict all of the scatter seen in the measurements, they certainly provide a possible explanation.

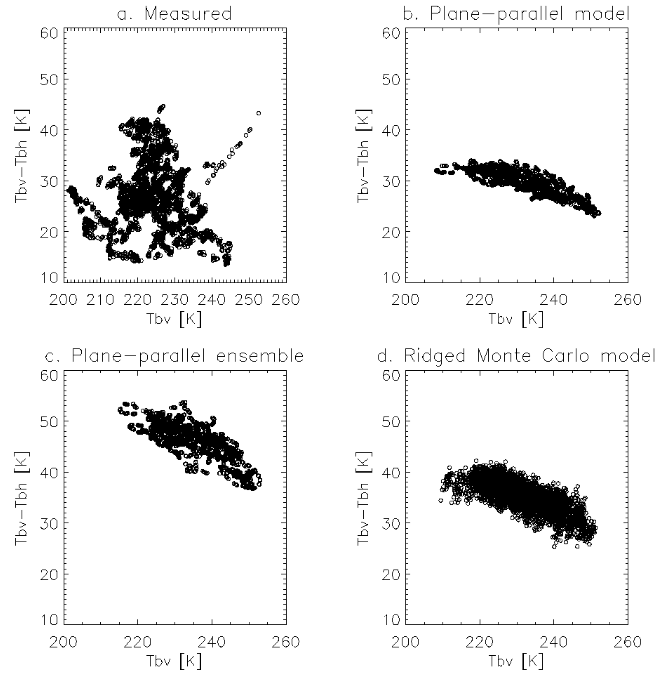

Fig. 19. Scatter plots of polarisation difference versus brightness temperature for measurements and model results of P3X to P2A overflights.

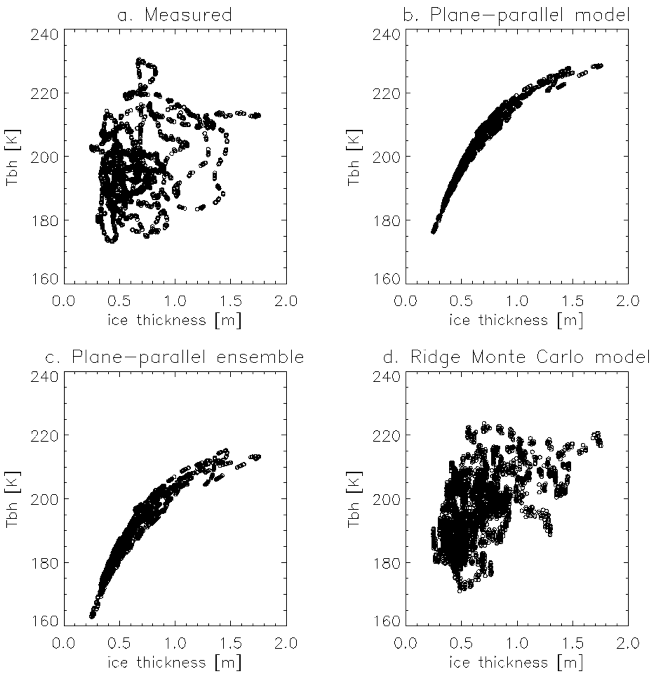

Fig. 20. Scatter plots of brightness temperature versus ice thickness for measurements and model results of P3X to P2A overflights.

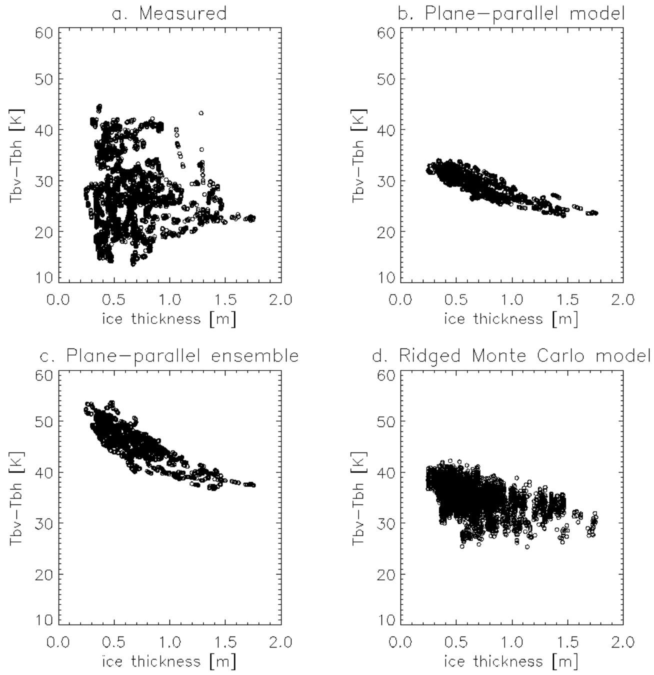

Fig. 21. Scatter plots of polarisation difference versus ice thickness for measurements and model results of P3X to P2A overflights.

It is clear that emissivity modelling of ice and snow pack is nowhere near the level of maturity of atmospheric radiative transfer models. Consider the following quote from a recent paper:

> Significant differences among the brightness temperatures and the extinction coefficients simulated with the four models in the cases of the six classes of snow are observed. Moreover, no particular model is found to be able to systematically reproduce all of the experimental data. The results highlight the need to more closely examine the relationships relating mean grain size and correlation length, introduce multiple layers in each model and to perform controlled laboratory measurements on materials with well-known electromagnetic properties in order to improve the understanding of the causes of the observed differences and to improve model performance [32].

The paper deals with modelling of layered snow-pack, however the basic challenges are the same and many of the same models are used.

Several challenges need to be overcome. One difficulty is the lack of ice core measurements collocated with radiance measurements. Most ice emissivity models are validated not on a point-by-point basis, as is customary for the majority of scientific study, but rather by comparing averaged measured radiances with brightness temperatures simulated from an averaged or idealized ice profile. When you consider the number of parameters input to a typical ice emissivity model—even the simple three-layer RT model has eight, at least two of which are quite difficult to determine—it becomes clear how much work is yet to be done. One way of dealing with the

TABLE I
CROSS-CORRELATION MATRIX FOR HORIZONTALLY POLARIZED BRIGHTNESS TEMPERATURES AND THE THREE EMISSIVITY MODELS USING THE EMPIRICAL THICKNESS-PERMITTIVITY RELATION.

	Measured	PP	Ensemble	MC
Measured	1.000	0.440	0.449	0.470
Plane Parallel	0.440	1.000	0.994	0.419
Ensemble	0.449	0.994	1.000	0.416
Monte Carlo	0.470	0.419	0.416	1.000

TABLE II
MATRIX OF PARTIAL CORRELATION COEFFICIENTS FOR HORIZONTALLY POLARIZED BRIGHTNESS TEMPERATURES AND THE THREE EMISSIVITY MODELS USING THE EMPIRICAL THICKNESS-PERMITTIVITY RELATION.

	Measured	PP	Ensemble	MC
Measured	1.000	-0.079	0.119	0.353
Plane Parallel	0.079	1.000	0.992	0.078
Ensemble	0.119	0.992	1.000	-0.044
Monte Carlo	0.353	0.078	-0.044	1.000

problem is to simply use satellite measurements, but because of the enormous size of a satellite footprint, there is no way that a single core sample will be in any way representative.

Another problem is relating ice bulk properties to emitted radiances. Even if we know temperature and salinity, we still need at least minimal knowledge of the micro-physical structure in order to calculate effective permittivity. This will be dealt with in the Section V-B. Finally, there may be other factors affecting sea ice emission not accounted for in these, highly idealized, models. While the previous sections have not shown conclusively that ice ridging is a factor, the next section will show statistically that it contributes significantly.

A. Ridged versus plane-parallel: detailed statistics

At first glance there appears little difference between the ridged models and the plane-parallel model. An examination of the cross-correlation matrix in Table I reveals a different story. While the ensemble of plane-parallel models are almost equivalent, the Monte Carlo model is less correlated with these two other models than it is with the measured values. This suggests that it generates information that the other two models do not, while losing some other piece. A model that combines the two types (plane-parallel and ridged Monte Carlo) should be more accurate than either alone.

Figure 22 shows the results of a ten-fold cross-validation regression analysis combining the single plane-parallel and ridged Monte Carlo models. The correlation coefficient, at 0.54, is significantly more than either alone thus confirming the hypothesis of the previous paragraph. A similar conclusion can be drawn from a matrix of partial correlation coefficients in Table II. Frequently employed in the social sciences, partial correlation measures the linear relation between two variables while controlling for one or more other variables. In the matrix, the pair of variables (row and column) are correlated after the effects of all other variables in the table are removed [33]. Now it can be seen how much extra information the Monte Carlo model supplies. The matrix also shows that

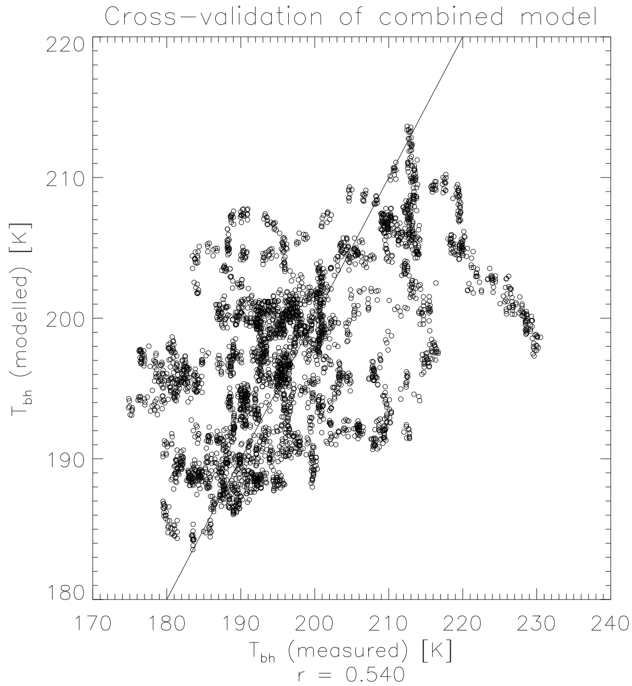

Fig. 22. Ten-fold cross-validation of multiple regression model relating plane-parallel and Monte Carlo emissivity models to measured sea ice brightness temperatures.

TABLE III
CROSS-CORRELATION MATRIX OF REAL PERMITTIVITIES CALCULATED FROM FIVE DIFFERENT FORMULAS.

	Vant	Sihvola	Shokr	Golden (mean)	SFT
Vant	1.00	0.998	0.979	0.744	0.716
Sihvola	0.998	1.00	0.983	0.744	0.722
Shokr	0.979	0.983	1.00	0.741	0.728
Golden (mean)	0.744	0.744	0.741	1.00	0.941
SFT	0.716	0.722	0.728	0.941	1.00

the ensemble refinement provides a small, but measurable improvement.

These results show that ice ridging makes a significant contribution to sea ice brightness temperature. The Monte Carlo model explains a part of the variance in the measured signal that the plane parallel models do not, but it does so at the expense of another part. In other words, neither model is complete. The Monte Carlo ridged model calculates emissivity using a geometric optics approach that is clearly inappropriate for the roughness scale relative to the wavelength: at around 20 cm, the wavelength is the same scale as the ridging. A more complete solution of Maxwell's equations, such as finite-difference modelling, would better account for the effect of ridging on the signal.

B. Comparison of modelled effective permittivities

A significant challenge to accurately modelling microwave emissivity of sea ice is the calculation of the dielectric constant. An analysis of the different mixing formulas reveals quite surprising differences between them and between the resulting calculated brightness temperatures. Figure 23 shows a comparison between three different mixture formulas, SFT and

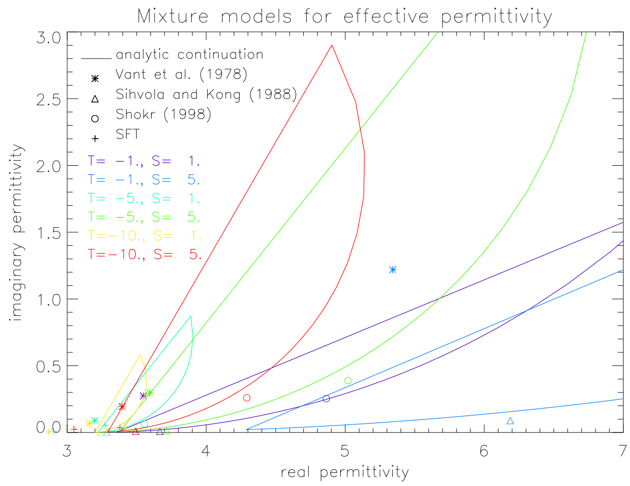

Fig. 23. Comparison of different mixture formulas for representative temperatures and salinities.

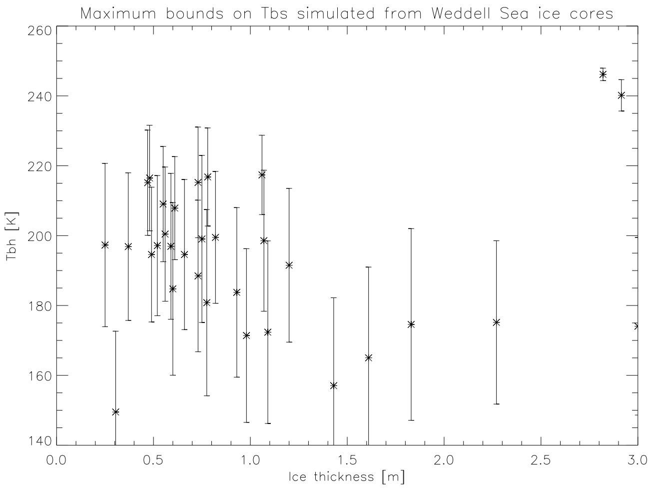

Fig. 24. Bounds on brightness temperatures modelled from ice cores taken in the Weddell sea for arbitrary brine geometry.

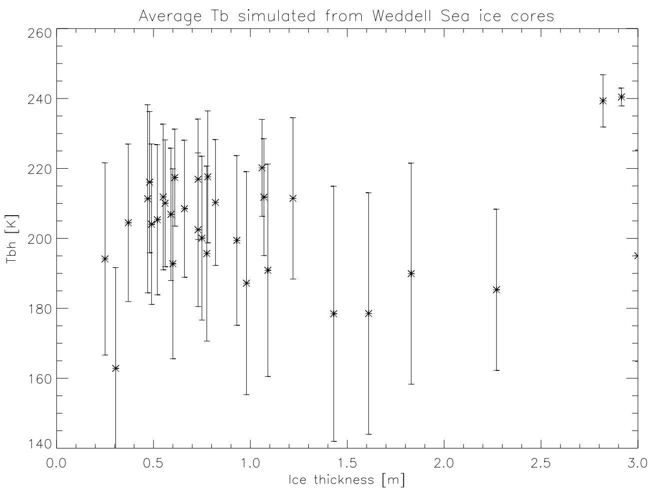

Fig. 25. Bounds on brightness temperatures modelled from ice cores in the Weddell sea using three different mixture formulas.

TABLE IV
CROSS-CORRELATION MATRIX OF IMAGINARY PERMITTIVITIES CALCULATED FROM FIVE DIFFERENT FORMULAS.

	Vant	Sihvola	Shokr	Golden (mean)	SFT
Vant	1.00	0.971	0.923	0.513	0.646
Sihvola	0.971	1.00	0.984	0.597	0.661
Shokr	0.923	0.984	1.00	0.637	0.646
Golden (mean)	0.513	0.597	0.637	1.00	0.828
SFT	0.646	0.661	0.646	0.828	1.00

the analytic continuation models. The three mixture formulas are the Vant model in Equation (11), Equation (5) from [15] for spherical inclusions:

$$\epsilon_{eff} = \epsilon_1 + \frac{3V_b(\epsilon_2 - \epsilon_1)\epsilon_2/(\epsilon_2 + 2\epsilon_1)}{1 - V_b(\epsilon_2 - \epsilon_1)/(\epsilon_2 + 2\epsilon_1)}, \qquad (33)$$

and Equation (18) from [16] for randomly oriented needles:

$$\epsilon_{eff} = \epsilon_1 + \frac{V_b(\epsilon_2 - \epsilon_1)}{3(\epsilon_2 + \epsilon^*)}(5\epsilon^* + \epsilon_2) \qquad (34)$$

where $\epsilon^* = \epsilon_1$ for $V < 0.1$ and $\epsilon^* = \epsilon_{eff}$ for $V_b \geq 0.1$. Note that *none* of the single calculations for effective permittivity fall inside of the analytic continuation bounds.

Figure 24 shows modelled brightness temperatures for 34 ice cores taken from the Weddell sea. These cores were gathered during cruises of the Polarstern and included profiles of temperature and salinity [28]. To get a maximal range of possible brightness temperatures, 100 runs of the radiative transfer model (Equations (5) and (6)) were performed, taking as input complex permittivities randomly chosen from along the analytic continuation bounds given by Equations (14) and (15). Averages are marked in Figure 24 by the stars while standard deviations are shown by the error bars.

The complex permittivity bounds used in the preceding analysis are constrained only by brine volume with no consideration given to geometry, so the results represent a maximal bound. If geometry were more constrained, the bounds would be smaller. Figure 25 shows a similar plot to Figure 24 except this time applying three different mixture formulas and taking the averages and standard deviations.

Even using only three different formulas, the results show a similar spread as using the maximally bounded analytic continuation method. More encouraging is the relatively good agreement between both the averages and the bounds: Pearson coefficients are 0.83 and 0.96 for the average vertically and horizontally polarized brightness temperatures respectively and 0.60 and 0.85 for the standard deviations. Scatter plots have been omitted since the relationship is quite clear by comparison of Figures 25 and 24. While the magnitudes of effective permittivity estimates vary along quite a broad spectrum, their functional form is quite similar as the cross-correlation matrices in Table III and Table IV illustrate.

It is also encouraging that mixture formulas for needles perpendicular to the field agree almost perfectly with the Vant empirical formulas (results not shown here) except for large values of brine volume. Brine pockets are typically elongated, with their longitudinal axes pointing vertically, along the direction of growth. For the horizontal polarization, we should use permittivity estimates for parallel, elongated inclusions where the field is perpendicular to the longitudinal axes of the inclusions. For the vertical polarization we need estimates in which the field is at an angle. In the Vant paper the authors appear to be using a horizontal field. In a later paper [34] whose results agree with Vant et al., however, the measurements appear to be taken with a fully vertical field, i.e. passing through the ice sheet from top to bottom.

VI. Conclusions

Coincident measurements of both the top and bottom ice surfaces along with L-band brightness temperatures were collected during the Pol-Ice campaign, conducted in March 2007 in the N. Baltic. The ice topography measurements were fed to three different ice emissivity models and the results compared with the radiance measurements. The models included a single, three-layer, plane-parallel radiative transfer (RT) model, an ensemble of plane-parallel RT calculations and a ridged, ray-tracing, Monte Carlo model that accounted for the topography of both the top and bottom surfaces of the ice using geometric optics. The models were described in detail in the body of the text including a derivation of the RT equations.

While the EMIRAD radiometer used during the campaign displayed calibration problems, particularly in the vertical channel, nonetheless it is believed that the relationships between modelled and measured brightness temperatures were meaningful. It is further hoped that the methods and concepts introduced will help improve sea ice microwave emissivity calculations at low frequencies such as L-band.

For the case studied, ice thickness was found to explain a significant proportion of the variance in brightness temperature—Figure 12. All models accurately accounted for the instrument antenna pattern, in the first by averaging thickness measurements over the footprint, in the second by averaging brightness temperature measurements and in the third by randomly varying the angle of a ray at the instrument head. Using the correct antenna pattern produced an improvement in the results and is highly relevant to satellite-mounted radiometers which sample a large and heterogeneous area.

As soon as we model the instrument as "seeing" over a broad footprint, rather than taking point measurements, variations in the ice sheet, such as ridging, become visible within a single measurement. It was found that ice ridging explains a small, but significant amount of the variance in the measured signal. While the Monte Carlo model had almost equivalent skill as the other two models as measured by Pearson correlation, a more thorough statistical analysis showed that it explains a portion of the variance in the measured signal that the other two do not and vice versa. A simulation of electromagnetic scattering more appropriate for the wavelength relative to the roughness scale is needed and would be a worthwhile extension to this study.

When a constant complex permittivity is assumed, the modelled polarisation difference is negatively correlated with the measured. To account for this negative correlation, it was assumed that the complex permittivity varies with ice thickness, albeit with large scatter. This relationship can be explained through ice growth processes. To determine it, effective permittivities were estimated by inverting the three-layer, plane-parallel RT model using collocated thicknesses and brightness temperatures. An exponential curve was then fitted. With the permittivity as a function of ice thickness, all three models showed improved correlation between measured and modelled polarization differences.

The campaign field data used in this study included only measurements of ice thickness and brightness temperatures. It is hoped that future studies might also include measurements of the internal properties of the ice. Permittivity values used in the models were only weakly related to the theory, primarily by comparison with analytic continuation estimates [18] which represent a maximum bound given unconstrained geometry. Other methods of generating single permittivity estimates based on either empirical estimates [6] or de-polarizability [15], [16] do not agree with analytic continuation, that is, they do not fall within the bounds. The explanation for this is not known. The calculation of effective permittivities is a significant obstacle to the accurate calculation of sea ice brightness temperatures, since knowledge of not just the ice bulk properties is required, but also knowledge of the ice micro-structural properties. Since the micro-structure of sea ice is complex, it is difficult to characterize in a quantitative way and therefore difficult to measure. The measurements must also be transformed into a form that is suitable for the theoretical models.

Acknowledgment

The authors would especially like to thank Stefan Hendricks for his help with the E-M bird thickness and altimetry data. Thanks also to Hajo Eicken for generously contributing Antarctic ice profile data. Cheers to other members of the SMOS-Ice project: Matthias Drusch and Catherine Bouzinac from the European Space Agency, Lars Kaleschke and Rasmus Tonboe. The authors would also like to thank Christian Maetzler and Mark Drinkwater.

References

[1] Y. H. Kerr, "Soil Moisture and Ocean Salinity: Radiometry applied to soil moisture and salinity measurements," CESBIO, 18 Avenue Edouard Belin 31401 Toulouse Cedex 4, France, Tech. Rep., November 1998, the Living Planet Programme Earth Explorer Missions.

[2] C. Maetzler, "Applications of SMOS over terrestrial ice and snow," in *Proceedings, 3rd SMOS Workshop*, DLR, Oberpfaffenhofen, Germany, December 2001.

[3] J. D. Menashi, K. M. St. Germain, C. T. Swift, J. C. Comiso, and A. W. Lohanick, "Low-frequency Passive-Microwave Observations of Sea Ice in the Weddell Sea," *Journal of Geophysical Research*, vol. 98, no. C12, pp. 22 569–22 577, December 1993.

[4] W. B. Tucker, D. K. Perovich, A. J. Gow, W. F. Weeks, and M. R. Drinkwater, "Physical Properties of Sea Ice Relevant to Remote Sensing," in *Microwave Remote Sensing of Sea Ice*, ser. Geophysical Monographs, F. D. Carsey, Ed. American Geophysical Union, 1992, no. 68, ch. 2, pp. 9–28.

[5] D. G. Barber, A. K. Fung, T. C. Grenfell, S. V. Nghiem, R. G. Onstott, V. I. Lytle, D. K. Perovich, and A. J. Gow, "The Role of Snow on Microwave Emission and Sacttering over First-Year Sea Ice," *IEEE Transactions on Geoscience and Remote Sensing*, vol. 36, no. 5, pp. 1750–1763, September 1998.

[6] M. R. Vant, R. O. Ramseier, and V. Makios, "The complex-dielectric constant of sea ice at frequencies in the range 0.1-40 ghz," *Journal of Applied Physics*, vol. 49, no. 3, pp. 1264–1280, March 1978.

[7] A. Stogryn, “A Study of Microwave Brightness Temperatures of Snow from the Point of View of Strong Fluctuation Theory,” *IEEE Transactions on Geoscience and Remote Sensing*, vol. GE-24, no. 2, pp. 220–231, March 1986.

[8] K.-P. Johnsen, “Radiometrische Messungen im arktischen Ozean–Vergleich von Theorie und Experiment,” Ph.D. dissertation, Universitaet Bremen, Otto-Hahn Allee 1, Bremen, Germany, 1998.

[9] T. J. Hewison and S. J. English, “Airborne Retrievals of Snow and Ice Surface Emissivity at Millimeter Wavelengths,” *IEEE Transactions on Geoscience and Remote Sensing*, vol. 37, no. 4, pp. 1871–1879, July 1999.

[10] K. Naoki, J. Ukita, F. Nishio, M. Nakayama, J. C. Comiso, and A. Gasiewski, “Thin sea ice thickness as inferred from passive microwave and in situ observations,” *Journal of Geophysical Research*, vol. 113, no. C02S16, 2008, doi=10.1029/2007JC004270.

[11] K. M. St. Germain, C. T. Swift, and T. C. Grenfell, “”determination of di-electric constant of young ice using microwave spectral radiometry”,” *Journal of Geophysical Research*, vol. 98, no. C3, pp. 4675–4679, 1993.

[12] Q. Liu, C. Simmer, and E. Ruprecht, “Monte Carlo simulations of the microwave emissivity of the sea surface,” *Journal of Geophysical Research*, vol. 103, no. C11, pp. 24 983–24 989, October 1998.

[13] C. Maetzler, Ed., *Thermal Microwave Radiation: Applications for Remote Sensing*. The Institution of Engineering and Technology, 2006.

[14] P. Hoekstra and P. Cappillino, “Dielectric Properties of Sea and Sodium Chloride Ice at UHF and Microwave Frequencies,” *Journal of Geophysical Research*, vol. 76, no. 20, pp. 4922–4931, July 1971.

[15] A. H. Sihvola and J. au Kong, “Effective Permittivity of Dielectric Mixtures,” *IEEE Transactions on Geoscience and Remote Sensing*, vol. 26, no. 4, pp. 420–429, July 1988.

[16] M. E. Shokr, “Field Observations and Model Calculations of Dielectric Properties of Arctic Sea Ice in the Microwave C-Band,” *IEEE Transactions on Geoscience and Remote Sensing*, vol. 36, no. 2, pp. 463–478, March 1998.

[17] F. T. Ulaby, R. K. Moore, and A. K. Fung, Eds., *Microwave Remote Sensing: Active and Passive, Volume III, From Theory to Applications*. Norwood, MA: Artech House, 1986.

[18] K. Golden, “Bounds on the complex permittivity of sea ice,” *Journal of Geophysical Research*, vol. 100, no. C7, pp. 13 699–13 711, July 1995.

[19] K. Golden and G. Papanicolaou, “Bounds for Effective Parameters of Heterogeneous Media by Analytic Continuation,” *Communications in Mathematical Physics*, vol. 90, pp. 473–491, 1983.

[20] N. Skou, S. S. Sobjaerg, and J. Balling, “EMIRAD-2 and its use in the CoSMOS Campaigns,” Electromagnetic Systems Section, Danish National Space Center, Technical University of Denmark, Tech. Rep. ESTEC Contract No. 18924/05/NL/FF, 2007.

[21] S. Hendricks and C. Haas, “L-Band Radiometry for Sea-Ice Applications: WP 2.2 Ice Thickness Deliverable Report,” Alfred Wegener Institute for Polar and Marine Research, Bremerhaven, Germany, Tech. Rep. ESTEC Contract N. 21130/08/NL/EL, January 2008, included as chapter in final report for SMOS-Ice project.

[22] G. Spreen, L. Kaleschke, and G. H. 2008, “Sea ice remote sensing using AMSR-E 89 ghz channels,” *Journal of Geophysical Research*, vol. 113, no. C02S03, 2008, doi=10.1029/2005JC003384.

[23] L. Kaleschke and N. Maass, “L-Band Radiometry for Sea-Ice Applications: WP 2.1 Campaign data analysis; WP 2.5 Ice concentration vs. ice thickness,” Institute of Oceanography, University of Hamburg, Tech. Rep. ESTEC Contract N. 21130/08/NL/EL, 2008, included as chapter in final report for SMOS-Ice project.

[24] M. Granskog, H. Kaartokallio, H. Kuosa, D. N. Thomas, and J. Vainio, “Sea ice in the Baltic Sea–A review,” *Estuarine, Coastal and Shelf Science*, vol. 70, pp. 145–160, 2006, doi=10.1016/j.ecss.2006.06.001.

[25] W. H. Press, S. A. Teukolsky, W. T. Vetterling, and B. P. Flannery, *Numerical Recipes in C*, 2nd ed. Cambridge University Press, 1992.

[26] W. F. Weeks and S. F. Ackley, “The growth, structure and properties of sea ice,” in *The Geophysics of Sea Ice*, ser. NATO ASI Series B: Physics, N. Untersteiner, Ed. Plenum Press, 1985, vol. 146, ch. 2.

[27] J. K. Ehn, B. J. Hwang, R. Galley, and D. G. Barber, “Investigations of newly formed sea ice in the Cape Bathurst polynya: 1. Structural, physical and optical properties,” *Journal of Geophysical Research*, vol. 112, no. C05002, 2007, doi=10.1029/2006JC003702.

[28] H. Eicken, “Salinity Profiles of Antarctic Sea ice: Field Data and Model Results,” *Journal of Geophysical Research*, vol. 97, no. C10, pp. 15 545–15 557, October 1992.

[29] R. Fuhrhop, C. Simmer, M. Schrader, G. Heygster, K.-P. Johnsen, and P. Schssel, “Study of Passive Remote Sensing of the Atmosphere and the Surface Ice,” Institute for Marine Science, Christian Albrechts University, Duestenbrooker Weg 20 D-24105 Germany, Tech. Rep. 297, 1997.

[30] M. Vancoppenolle, C. M. Bitz, and T. Fichefet, “Summer landfast sea ice desalination at Point Barrow, Alaska: Modeling and observations,” *Journal of Geophysical Research*, vol. 112, no. C04022, 2007, doi=10.1029/2006JC003493.

[31] S. Martin, R. Drucker, R. Kwok, and B. Holt, “Improvements in the estimates of ice thickness and production in the Chukchi Sea polynyas derived from AMSR-E,” *Geophysical Research Letters*, vol. 32, no. L05505, 2005, doi=10.1029/2004GL022013.

[32] M. Tedesco, E. J. Kim, A. W. England, R. D. Roo, and J. P. Hardy, “Intercomparison of Electromagnetic Models for Passive Microwave Remote Sensing of Snow,” *IEEE Transactions on Geoscience and Remote Sensing*, vol. 44, no. 10, October 2006.

[33] M. Kendall and A. Stuart, *The Advanced Theory of Statistics*, 3rd ed. MacMillan, 1973.

[34] S. A. Arcone, A. J. Gow, and S. McGrew, “Structure and Dielectric Properties at 4.8 and 9.5 GHz Saline Ice,” *Journal of Geophysical Research*, vol. 91, no. C12, pp. 14 281–14 303, December 1986.

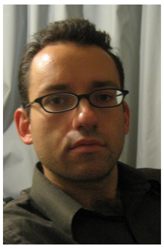

Peter Mills was born on December 22, 1973 in Montreal, Canada. He received his Bachelor’s Degree in Physics from the University of Waterloo in Ontario, Canada and a Master’s Degree in Environmental Physics from the University of Bremen, Germany. He has a passion for all forms of rational inquiry, particularly those that cross disciplines. Examples include chaos theory, artificial life, complexity theory and cognitive science. He has authored two papers on chaos theory.

Georg Heygster Georg Heygster (M’00) received the Diploma degree in solid-state physics and the Ph.D. degree in digital image processing from the University of Göttingen, Göttingen, Germany, in 1976 and 1979, respectively.

He served as a Consultant with the Computer Center of the University of Bremen, Bremen, Germany, from 1979 to 1988. Since then, after working for a year on the imaging mechanisms of scanning acoustic microscopes, he has been Head of the Geophysical Analysis of Satellite Images group at the Institute of Environmental Physics, University of Bremen. His research activities include passive and active microwave remote sensing, particularly of both surface and atmospheric parameters in the high latitudes, various aspects of the hydrological cycle, long-term trends, and retrieval techniques. He was or still is Principal Investigator or Coinvestigator of many research projects funded by the European Union, the European Space Agency, the German Research Council, and the Japan Aerospace Exploration Agency. These projects include the development of sensor soft- and hardware, conducting campaigns, the final data analysis from multi- and single-sensor data to geophysical parameters, and the interpretation and application of these results in many areas such as meteorology, climatology, and oceanography.